

# Plasmonic Gradient Arrays for Rapid Screening of Surface-Enhanced Raman Scattering Efficiency: Particle Libraries of Gold Nanostars

Christian Kuttner,\* Valentina Piotto, and Luis M. Liz-Marzán\*



Cite This: <https://doi.org/10.1021/acs.chemmater.1c03223>



Read Online

ACCESS |



Metrics & More

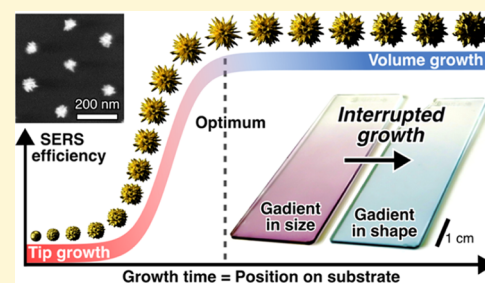


Article Recommendations



Supporting Information

**ABSTRACT:** The efficiency of signal enhancement for surface-enhanced Raman scattering (SERS) spectroscopy is a crucial parameter for the design and development of nanoparticle-based sensing applications. However, screening SERS capabilities of anisotropic nanoparticles by iterative synthesis is time consuming, and their prediction still suffers from the complex nonlinear relationships of morphological and electromagnetic properties. We present an approach to use a macroscopic gradient array of substrate-supported nanoparticles for rapid screening of their SERS efficiencies. The gradient represents a “plasmonic library” of colloids synthesized by two-step post-modification of a monolayer of randomly close-packed gold nanospheres covered with poly(*N*-isopropylacrylamide) shells. A first chemical overgrowth process yields a continuous gradient of seed particles, with diameters ranging between 10 and 60 nm. Subsequently, the seeds are further grown into nanostars (NSs) with spiky tips, which improve their SERS-enhancing capabilities. Raman mapping along the gradient provides rapid and reliable quantification of the specific SERS efficiencies for the whole library, as well as correlation of their optical and structural properties. By ensuring that the number and density of particles in the Raman excitation volume remain constant, the most appropriate synthetic conditions for efficient SERS can be readily identified on a single screening. As a proof of application, we screened the SERS performance of a library of NSs and applied the selected best candidates for the detection of the bacterial biomarker pyocyanin. This bacterial quorum sensing signaling molecule was quantitatively detected within a linear dynamic range between  $10^{-7}$  and  $10^{-5}$  M, suitable for clinical applications.



## INTRODUCTION

Gold nanostars (NSs) have become an important element for various photonic applications,<sup>1–3</sup> among which their use as ultrasensitive chemical sensors in surface-enhanced Raman scattering (SERS) spectroscopy is arguably the most prominent one.<sup>4,5</sup> These branched colloids, also known as nanoflowers or multipods, follow the *leitmotif* of a central core, which acts as an antenna for light due to its significant absorption cross-section, and several radially protruding arms with pointed tips.<sup>6</sup> Because of the efficient energy transfer between these conceptual building blocks, the tips can generate largely enhanced electric near-fields that amplify the Raman scattering of adsorbed molecules.<sup>7</sup> The optical properties of NSs are governed by a broad absorbance band, a convolution of various hybridized modes from coupled core and tip plasmons,<sup>7</sup> usually located in the near-infrared (NIR). As such, gold NSs are promising candidates for non-invasive nanomedical applications in the first NIR transparency window of biological tissue, as for example, photothermal cancer therapy,<sup>8,9</sup> or the detection of biomarkers<sup>10</sup> of bacterial infections.

SERS substrates with 2D particle arrangements can be roughly divided into two kinds of designs; comprising either close-packed or spaced (isolated) particles. Although the latter kind relies exclusively on the primary hotspots of each particle, dense multi-particle assemblies may offer additional secondary

hotspots with higher field enhancement, generated in the minute gaps between neighboring particles.<sup>11</sup> However, for dense arrangements of NSs, an attenuation of the near-fields by perturbing plasmonic interactions has been observed and calculated.<sup>12,13</sup> This “deactivation” of hotspots is a limiting factor for SERS efficiency and favors spatially separated, plasmonically decoupled NSs. For other morphologies (spheres, rods, triangles, *etc.*), this effect is more subtle and, in most cases, coupled particles still offer superior performance to isolated particles.<sup>13</sup> Notwithstanding, NSs offer significantly higher inherent enhancement factors ranging from  $10^4$  to  $10^7$  ( $10^{10}$  on Au mirror<sup>16</sup>), depending sensitively on tip geometry<sup>17</sup> and excitation conditions.<sup>18</sup> Therefore, SERS substrates with isolated NSs appear as a viable option for “sensing pixels.”

For a NS to be detectable as an independent “sensing pixel,” fairly large separation distances are required, due to the diffraction limit ( $0.5 \lambda/\text{NA} \approx 300\text{--}400$  nm, for  $\lambda = 633$  or 785

Received: September 17, 2021

Revised: October 15, 2021



nm and  $NA = 1$ ). However, to function as plasmonically independent objects, that is, decoupled from their nearest neighbors, shorter spacings of  $\approx 1$ – $2$  times their effective diameter are sufficient. Such a spatial control can be achieved by incorporating a dielectric spacer, for example, a shell made of mesoporous silica<sup>19</sup> or a polymer.<sup>20,21</sup> However, the direct encapsulation of branched nanoparticles by seeded precipitation polymerization is challenging because elevated temperatures result in dulled tips by reshaping<sup>22</sup> and thus reduced SERS efficiency. For that reason, it is preferable to use Au nanoparticles that have been pre-encapsulated<sup>23</sup> with poly(*N*-isopropylacrylamide) (pNIPAM), as seeds for the solution-based growth of NSs.<sup>24</sup>

By means of colloidal fabrication methods, such as microgel particles with NS cores can be organized on solid supports as either close-packed monolayers or patterned structures,<sup>24</sup> for example, using template-assisted self-assembly. Alternatively, substrate-immobilized NSs can be obtained from substrates hosting seed arrays. Demille *et al.* recently demonstrated the synthesis of NSs using near-hemispherical Au structures as substrate-bound seeds.<sup>25</sup> These seed structures were prepared from a template with cylindrical holes obtained by nanoimprint lithography, deposition of Au/Sb by sputtering, template lift-off, and thermal reshaping of the resulting disks into quasi-hemispheres with diameters of *ca.* 65 nm. Notably, these seeds are significantly larger than those commonly used in solution-based syntheses (10–15 nm), as mentioned above. It should be noted that seed size is known to play an important role in the growth kinetics of branched nanoparticles.<sup>26</sup>

In a lithography-free colloidal approach, close-packed monolayers of pNIPAM microgels with spherical Au cores could serve as arrays of isolated seeds.<sup>27</sup> However, so far only the growth of dense arrays of branched Au nanostructures from substrate-immobilized colloidal seeds has been explored,<sup>28</sup> whereas the growth of isolated NSs has not. In 2014, Müller and co-workers demonstrated the isotropic overgrowth of seed arrays into a “plasmonic library” of Au nanospheres with a macroscopic, continuous gradient in size from 10 to 60 nm by “interrupted growth”.<sup>29</sup> The process involved dip-coating (controlled immersion and pull-out) of a seed array in a growth solution, which resulted in seed overgrowth tuned by local exposure time. Later, Sindram *et al.* developed a synthesis route for the controlled interrupted overgrowth of seed arrays with Ag, maintaining their spherical morphology and low size dispersion.<sup>30</sup> Such plasmonic libraries have been proposed as platforms for combinatorial screening of size effects, for example, in catalysis,<sup>31</sup> plasmon coupling,<sup>32</sup> or fluorescence enhancement.<sup>30</sup>

Gradient screening arrays, hosting a library of particles, could also help resolve transitions in optical and morphological properties during fast growth processes, such as the autocatalytic anisotropic growth of NSs. The study of transient properties of intermediate states in solution-based synthesis is challenging as taking aliquots requires a fast removal of the growing particles from the growth medium. The high workload involved in the study of a series of transient states renders detailed kinetic studies impractical. Seed arrays in combination with interrupted growth by dip-coating allow “freezing” a continuous series of transition states along the gradient, which could be readily analyzed with little practical effort. Similarly, the optimization of SERS substrates by iterative adaptation of plasmonic properties is a time consuming and tedious task. Indeed, the workload involved in tailoring plasmonic SERS

substrates to a specific excitation wavelength is immense and generally results in a trade-off between excitation efficiency and signal enhancement.

Here, we demonstrate that gradient arrays are a useful tool for rapid screening of SERS efficiency and its correlation with optical and morphological properties. This is exemplified by the plasmonic tailoring of substrate-immobilized NSs for two excitation lines, 633 and 785 nm. We first identified the best enhancement conditions using 4-nitrothiophenol (NTP) as a low-molecular-weight model analyte. Then, as a proof-of-concept application, the substrates were applied to the SERS detection of pyocyanin (PCN<sup>-</sup>), a quorum sensing signaling molecule and biomarker for bacterial infections by *Pseudomonas aeruginosa*. PCN<sup>-</sup> is a challenging biomarker owing to its weak adsorption affinity onto Au surfaces. Therefore, we exploited the thermo-responsive properties of the pNIPAM spacers to function as a molecular trap<sup>24,33</sup> for the collection of the hydrophobic biomarker molecules from solution.

## RESULTS AND DISCUSSION

### NS Growth from Substrate-Immobilized Seeds.

Gradient arrays formed by “interrupted growth” of immobilized seeds enable the acquisition of a continuous series of transient states and their convenient analysis after synthesis. To exemplify this for the growth of isolated substrate-supported NSs, we first prepared monolayers of pNIPAM microgels with quasi-spherical Au cores as seed arrays (Figure 1a) by spin-coating a concentrated aqueous dispersion (1 wt %) on poly(ethylenimine) (PEI)-coated microscopy glass slides (see [Materials and Methods](#) for experimental details).<sup>30</sup> The PEI coating serves as an adhesion promoter to prevent particle detachment during multi-stage processes. The size of cores obtained by citrate reduction was approx. 12 nm. After encapsulation by free-radical precipitation polymerization,<sup>23</sup> the overall hydrodynamic diameter increased to an average of 275 nm at 20 °C, as determined by DLS (Figure S2a). The resulting monolayers were washed with EtOH and dried. AFM images revealed the presence of a single-particle layer with random close-packed domains and a homogeneous particle density of  $27 \pm 1 \mu\text{m}^{-2}$  (Figure S3a). The pNIPAM shells acted as soft spacers that kept the seeds at a minimum center-to-center distance  $d_{cc}$  of 190–200 nm, as demonstrated by statistical analysis using a pair-correlation function (Figure S3b). This spacing is sufficient to prevent plasmonic coupling and near-field interactions between neighboring particles. The prepared glass substrates appeared transparent with a slight pink hue (Figure 1b). Prior to anisotropic Au overgrowth, the substrates were incubated in a 10 mM solution of polyvinylpyrrolidone (PVP, 10 kg mol<sup>-1</sup>) in *N,N*-dimethylformamide (DMF) for pre-functionalization of the immobilized seeds.

The substrates were then mounted on a dip-coater and immersed into a PVP/DMF growth medium containing 0.275 mM HAuCl<sub>4</sub>. The growth process with substrate-immobilized seeds is in principle identical to the solution-based synthesis, as reported by Mueller *et al.* (Section S1),<sup>24</sup> except that we avoided any potential seed oxidation. Immersion was therefore not initiated until the gold precursor had been completely pre-reduced to Au(I), as followed by UV/vis spectroscopy (Figure S1f). After rapid immersion, the substrate was pulled out at a constant rate of 1 mm min<sup>-1</sup>. This vertical sample movement made it possible to interrupt the growth and thus control the time during which the seeds were exposed to the growth

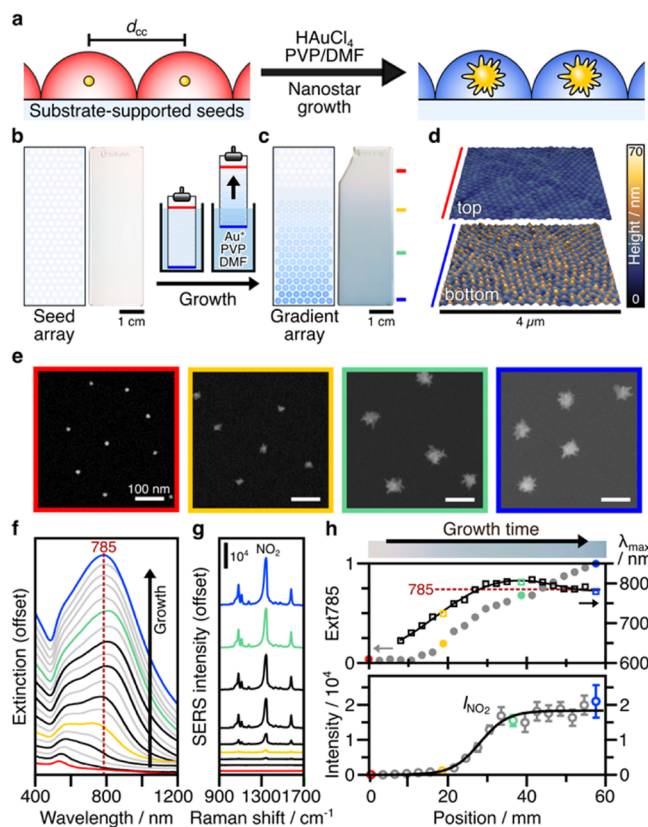


**Figure 1.** Growth of NS gradient arrays from substrate-supported seeds. (a) Schematic depiction of the growth process. (b) Gradient fabrication on macroscopic areas by interrupted growth of a seed array of Au/pNIPAM core/shell particles, continuously pulled-out from a PVP/DMF growth medium. (c) Gradual transition from colorless to blue, from top to bottom. (d) AFM topography images for the opposite ends of the gradient: top (red mark, no contact to the growth solution) and bottom (blue mark, longest time in the growth solution). (e) Corresponding SEM images at exemplary positions. (f) Spectral evolution of NS growth measured along the gradient and (g) corresponding SERS spectra [red, green, orange, blue, and black lines in (f)]. (h) Correlation of optical properties (extinction at 785 nm and LSPR maximum) and SERS intensity using 785 nm excitation, obtained from Raman mapping ( $20 \times 20 \mu\text{m}^2$ ) along the gradient. The gain in SERS efficiency coincides well with the optical changes (LSPR red-shift toward 785 nm), in agreement with the formation of tips/spikes on the seeds.

solution. Thus, particles on the upper part of the substrate spent the shortest time inside the growth medium (red mark in Figure 1b), whereas those on the bottom were exposed for the longest time (blue mark, 60 min). The true exposure time comprises the time of immersion and a delay caused by the moving meniscus. Growth is expected to stop at the point where evaporation of water causes the pNIPAM shells to collapse tightly onto the cores, separating them from additional gold ions—and thus “freezing” the growing species.

The change in plasmonic properties and their gradual progression along the pull-out direction is readily visible to the naked eye (Figure 1c). From the upper part, the color changes from colorless through pink to light blue and blue at the bottom. AFM topography analysis at both ends of the gradient shows clear differences (Figure 1d). While the upper section, corresponding to the initial state, is dominated by the collapsed shells, the bottom section shows the presence of larger, edgy cores emerging from the microgel (for a detailed view, see

Figure S4). However, AFM only allows making a preliminary conclusion on the formation of branched cores. Scanning electron microscopy (SEM) is better suited to study the core morphology and its transition from sphere to star. Figure 1e shows images from four sample positions, assigned to the colors red, yellow, green, and blue (see marks in Figure 1c), to demonstrate the effect of longer growth times. Here, we highlight two intermediate steps, namely, the point at which the first tips became visible (orange mark, 20 min) and the point at which growth stagnates and tip formation appeared to be completed (green mark, 40 min). Comparing the latter with the final morphology (blue mark), the NSs seem to be of similar size though somewhat bulkier.

For the optical characterization, we performed UV/vis/NIR spectroscopy in the dry state. The results of 19 positions along the gradient are shown in Figure 1f. The measured area, given by the beam size in the spectrometer, was  $7 \times 1.3 \text{ mm}^2$ . The first spectrum (red color) corresponds to the seed array with quasi-spherical particles and a weak plasmon resonance at 525 nm. Thereupon, the gradual formation of the main (tips) plasmon band around 785 nm and the secondary (core) mode at 550–560 nm can be monitored.

To quantify SERS performance, we labeled the gradient substrate with NTP, a low-molecular-weight model analyte with high binding affinity to gold surfaces. In addition, NTP's moderate polarity renders it partly soluble in water, in contrast to many other commonly used insoluble Raman markers. Labeling was carried out by overnight immersion in a  $1 \mu\text{M}$  aqueous NTP solution, followed by washing with water and drying. The substrate was then measured stepwise by mapping areas of  $20 \times 20 \mu\text{m}^2$  (121 points) at equidistant intervals along the gradient direction. The SERS efficiency is based on the overlap of the excitation light with the nanostructure's plasmon band. For many systems, for example, for single particles, SERS intensity peaks at resonant excitation. In contrast, nanostructures with coupled plasmons, including multi-particle assemblies and hierarchical superstructures,<sup>34–36</sup> have been shown to be most efficient at non-resonant conditions. In the case of isolated NSs, however, we expected the highest SERS efficiency at an excitation in resonance with the plasmon band.<sup>37</sup> Therefore, we used an excitation laser at 785 nm. Figure 1g shows selected spectra in a stacked representation (according to the color scheme introduced in Figure 1f). Initially, SERS activity is negligible, as is to be expected for isolated gold nanospheres (red).<sup>38</sup> In the reaction time window of 20–40 min (orange to green), SERS intensity increased significantly and allowed reliable detection of NTP, even at low integration times of 1 s. At later growth times (green to blue, 40–60 min), the SERS enhancement increased only marginally, in-line with the observed minor optical changes (Figure 1f). These results further suggest that the tips were fully grown at the start of this last growth phase.

Since the gradient substrate contains a library of NS intermediates, this system allows a direct correlation of optical properties (top, Figure 1h) and SERS efficiency (bottom). The optical data are composed of the extinction at the excitation wavelength (Ext785, closed circles) and the spectral position of the localized surface plasmon resonance (LSPR) band ( $\lambda_{\text{max}}$ , open squares). The SERS efficiency ( $I_{\text{NO}_2}$ , open circles) indicates the intensity of the  $\text{NO}_2$  stretching vibration in NTP, at  $1340 \text{ cm}^{-1}$ . Since the number of particles probed in the finite excitation volume (spot area  $\approx 2.9 \mu\text{m}^2$ ) is defined and

constant ( $27 \pm 1 \mu\text{m}^{-2}$ ), the detected intensity indeed reflects the efficiency of SERS generation at each intermediate state. Up to 20 min (orange mark), the growing seeds display negligible SERS activity, even though both optical and SEM data indicate that anisotropic growth, that is, the nucleation of branches, already started at that time. The lack of SERS activity thus results from disadvantageous features such as poorly developed tips and a small core size that cannot act as an efficient antenna due to a low absorption cross section. In this first growth phase, the increase in the size of the seeds is relatively slow because the formation of branches relies on the reduction of gold ions at the seed surface. The second phase is dominated by branch growth, evidenced by the rapid red shift of the plasmon band from 650 to 800 nm within 10 min, accompanied by a progressively increasing extinction cross-section (Ext785). These optical changes coincide with the increase in SERS activity. At the transition to the last growth phase (green mark), dominated by isotropic overgrowth,<sup>39</sup> the formation of branches is completed and the maximum SERS activity is reached. At the same time, the redshift of the plasmon band comes to a halt and even a shallow plateau can be observed for the increase in extinction (Ext785). The latter is only weakly pronounced since the subsequent blue shift from 800 nm back to 785 nm leads to a further increment of the Ext785 value. Such a blue shift indicates the transition from anisotropic to isotropic overgrowth, which will cause a dulling of the tips. We could not observe this effect by SEM due to limited resolution. The tendency of sample surfaces to accumulate charge limited the available accelerating voltage and thus the beam resolution (see [Materials and Methods](#)). Detailed investigation of the evolution of the tip morphology will be considered in further studies, but this is beyond the scope of this work. Nevertheless, we note that absolute extinction at 785 nm alone is not a reliable indicator for predicting SERS efficiency. In contrast, SERS analysis reveals a sigmoidal evolution of the enhancement and an eventual saturation after 40 min of growth.

Hereby, we exemplified the advantages of gradient arrays for acquisition of intermediate states and their convenient analysis. Notably, since the SERS-active species are confined to a 2D arrangement, the position of the focal plane is of utmost importance ([Figure S5](#)). This is also reflected in the error bars ([Figure 1h](#), bottom), which are at least partially affected by a possible variation of the focus. In fact, correct focusing could be a key instrumental challenge for fast screening and reliable readout of gradient arrays.

**NS Growth from Gradient Seed Arrays.** Next, we demonstrate the influence of seed size on branching by using seed arrays with a size gradient. In this way, the effect of a rapid growth of the core during the branching process can be reproduced experimentally. For this purpose, growth was performed in two steps ([Figure 2a](#)): first, an isotropic overgrowth to increase seed size; followed by anisotropic overgrowth to form NSs, as described above. Seed size adjustment is also an option for plasmon tuning, by controlling the core size of NSs, for example, for efficient excitation tailored to 633 nm.

By interrupted isotropic overgrowth, a substrate-immobilized array with homogeneous small seeds ([Figure 2b](#)) was converted into a seed array with a continuous gradient in size ([Figure 2c](#)). To this end, the array was immersed into a growth solution containing cetyltrimethylammonium bromide (CTAB, 0.1 M) and HAuCl<sub>4</sub> (0.41 mM, final concentration), pre-

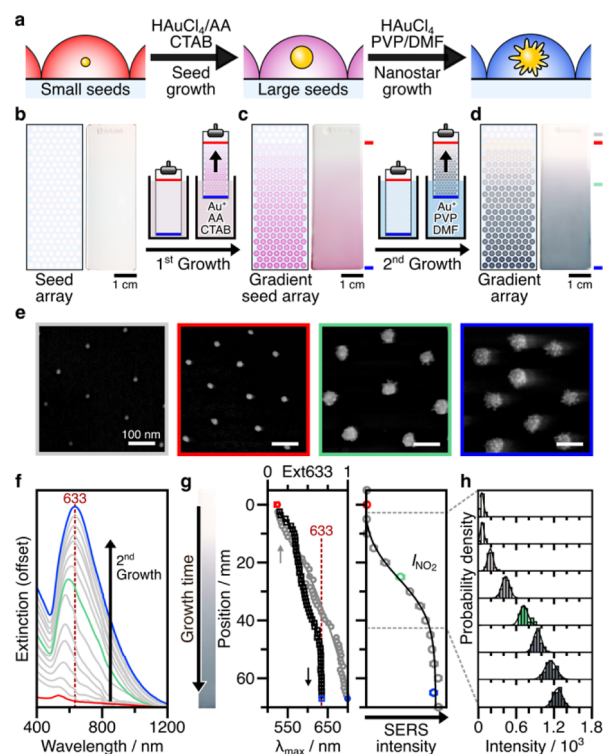


**Figure 2.** Growth of NS gradient arrays from gradient seed arrays. (a) Schematic depiction of the two-step growth process. Conversion of a seed array (b) to a gradient seed array (c) by interrupted growth, using an AA/CTAB growth medium. (d) Overgrowth into NSs by interrupted growth using a PVP/DMF growth medium. (c) Gradual transition from transparent to blue, from top to bottom. (e) TEM images at selected positions of the NS gradient [gray, red, green, and blue lines in (d)]. (f) Spectral evolution of the NS growth measured along the gradient. (g) Correlation of optical properties (extinction at 633 nm and LSPR maximum) and SERS intensity using 633 nm excitation, obtained from Raman mapping ( $20 \times 20 \mu\text{m}^2$ ) along the gradient. (h) Detailed view of the sigmoidal increase in SERS efficiency.

reduced by a weak reducing agent ascorbic acid (AA, 0.1 M). Then, the local reaction time was controlled by pulling out the substrate at a rate of  $1 \text{ mm min}^{-1}$ . In this way, a continuous gradient in particle sizes from 12 to 65 nm in diameter was obtained, as described in full detail by Müller et al.<sup>29,32</sup>

This size gradient corresponds to a gradient in LSPR maximum from 525 nm (top, red mark) to 550 nm (bottom, blue mark). A transition from transparent pink to intense pink can again be seen with the naked eye ([Figure 2c](#)). After repeated washing with water to remove residual growth medium and after pre-functionalization with PVP, interrupted anisotropic overgrowth was performed, as described above. By using the same pull-out rate, particles spent an identical time in each growth solution. The coloring of the resulting array ranged from transparent pink through light violet to dark blue ([Figure 2d](#)).

[Figure 2e](#) shows SEM images of four exemplary sample positions, assigned to the colors gray, red, green, and blue (see marks in [Figure 2d](#)), with increasing seed sizes: gray represents the initial seeds which were neither isotropically nor anisotropically overgrown; red corresponds to particles at the upper end of the gradient, which spent the shortest time inside the growth solution, with a size of 15–20 nm and a quasi-spherical shape without visible branching; green depicts

particles after 25 min of growth, with large cores of 30–40 nm and short protruding tips; blue shows particles at the lower end of the gradient with core sizes of 60–65 nm and visibly populated by several short tips. An extended overview of SEM images from 15 equidistant positions over the entire gradient is shown in Figure S6. All intermediate growth stages are characterized by low aspect ratio branches (projection length vs particle diameter). As described by Song *et al.*,<sup>39</sup> the size of the seed controls the ratio of branch nucleation and branch growth. By progressively enlarging the surface area of seeds during growth, nucleation of additional branches is promoted at the expense of branch growth.

Due to the small aspect ratio of the branches, the plasmon band does not shift into the NIR range. Figure 2f depicts the evolution of the plasmon band, characterized by a narrower red shift from 530 nm (red) to 590 nm (green) to 633 nm (blue). The plasmon band is a convolution of contributions from the core and the tips. Especially in the initial growth steps (red to green), the core mode dominates the optical properties, which is reflected in an asymmetric band shape. Subsequently (green to blue), the tip contributions become more prominent.

To quantify SERS performance, we labeled the substrate with 1  $\mu\text{M}$  NTP and performed Raman mapping along the gradient using a HeNe laser at 633 nm for excitation. Figure 2g shows a direct correlation of optical response (left) and SERS efficiency (right). Again, the extinction at the excitation wavelength (Ext633, gray circles) alone is a poor indicator for predicting the SERS efficiency of intermediate species. The average intensity follows a sigmoidal behavior with a turning point represented by the green circle and a saturation after ca. 40 min of growth. The maximum gain is reached at the point where the plasmon resonance (Figure 2g, black squares) coincides with the excitation line. Notably, the variation in SERS intensities is below 5% (standard deviation, Figure 2h). We could observe that the antenna character is indeed a function of the core size since the observed signal stability depended critically on laser power (Figure S7). This dependence can be attributed mainly to NSs suffering from reshaping/dulling upon photothermal heat generation,<sup>22</sup> as indicated by a color change at the illuminated areas, from blue to pink. To evaluate the reliability and repeatability of the sample readout, we tested different power densities and illumination times: At  $1.8 \pm 0.5 \text{ mW } \mu\text{m}^{-2}$ , the SERS intensity halved within 2 min of illumination; in contrast, at  $0.2 \text{ mW } \mu\text{m}^{-2}$ , which was the maximum power density used for Raman mapping, as shown in Figure 2, the intensity decreased by less than 10% after 15 min, which we consider appropriate for analytical screening applications.

**Combinatorial Screening of Synthesis Parameters.** In the previous sections, the time dependence of branch formation (Figure 1) and the influence of seed size (Figure 2) were investigated using experiments with interrupted growth, in which the precursor concentration was kept constant (0.275 mM). However, the ratio of Au<sup>+</sup> ions to seeds' surface area is an essential factor to define branching kinetics in gold NSs. To demonstrate the use of gradient particle arrays for combinatorial screening, we varied the concentration of Au in the growth solution between 0.055 and 0.825 mM (final concentration) in 15 uniform steps. Growth was performed in this case by immersion without interruption by extraction (Figure 3a). Based on the correlations, as shown in Figure 1h, we limited the immersion time to 30 min, followed by 5 min of washing and drying. This procedure

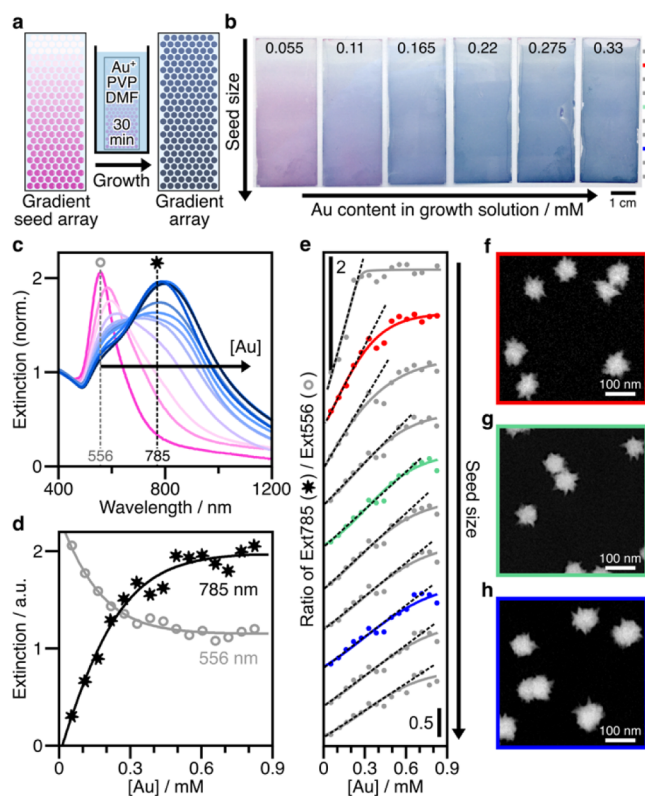


**Figure 3.** Influence of Au content and seed size on the kinetics of NS growth. (a) Schematic depiction of overgrowth by uninterrupted immersion of gradient seed arrays. (b) Resulting gradient arrays after 30 min for PVP/DMF growth solutions with various Au contents. (c) Exemplary change in optical properties at position 2 from the top (red marker) and corresponding (d) spectral evolution of the contributions of core (556 nm, grey circles) and tips (785 nm, black asterisk). (e) Kinetics of the gradual morphological change from spheres to stars, indicated by the ratio between extinction at 785 and 556 nm, for various seed sizes (see b, for positions) and as a function of Au content (stacked representation for visibility, black dashed lines serve as guides to the eye). (f–h) SEM images of NSs at three exemplary positions, at the top (red), middle (green), and bottom (blue) along the gradient arrays (0.6 mM).

ensured that growth was interrupted after the branching phase and before the subsequent phase of isotropic residual growth.

Figure 3b shows six exemplary substrates (0.055–0.33 mM) resulting from the 15 parallel experiments, using separate reaction media of 30 mL (for details see Materials and Methods). Pre-reduction of gold ions was performed in a common batch and then diluted with PVP/DMF (10 mM) to avoid differences in reactivity by composition, mixing, aging, and so forth. A gradient in color is visible both along each substrate (top to bottom) and when comparing the series of samples side by side. At the lowest Au content (0.055 mM), the sample retains a pink–violet color, whereas other samples gradually turn blue as the concentration increases. The optical properties of each substrate were recorded at 10 fixed positions (see marks in Figure 3b) using a uniaxially translating sample holder. The spectral response to the available Au content in the synthesis can thus be illustrated for each of the 10 analyzed seed sizes along the gradient array, as exemplified by Figure 3c at position #2 from the top (red mark). With increasing precursor concentration, the main mode shifts from 556 to 785 nm. The first spectrum (pink, 0.055 mM) corresponds to seeds

that grew into ill-defined, polydisperse, faceted particles showing no branches or tips. Here, the supply of Au ions was insufficient to promote branching by anisotropic overgrowth. Figure 3d illustrates the conversion from non-branched (gray circles) to branched particles with well-developed tips (black asterisks) by the evolution of their characteristic wavelengths. Above the crossing point ( $>0.25$  mM), the higher-wavelength contributions by the tip modes to the LSPR band become dominant over the lower-wavelength contributions from the core modes. Therefore, the extinction ratio ( $\text{Ext}_{785}/\text{Ext}_{556}$ ) can be employed as a first-order estimate of the conversion efficiency and the susceptibility of each seed size to branching under the different compositions of the growth media (Figure 3e). The stacked representation indicates that the branching susceptibility  $\chi_{\text{branch}}$  (dashed black line) is a function of both the supply of Au ions [Au] and the seed surface area  $A_{\text{seed}}$  available for autocatalytic reduction.

$$\chi_{\text{branch}} = \frac{\text{tip growth}}{\text{volume growth}} \approx \frac{\text{Ext}_{785}}{\text{Ext}_{556}} \propto \frac{[\text{Au}]}{A_{\text{seed}}} \quad (1)$$

This analysis permits to estimate the appropriate Au concentration to promote the growth of NSs for 785 nm excitation, from seeds of various sizes. Whereas small seeds of 12 nm only require low concentrations of about 0.25 mM (c.f. Figure 1), larger seeds require a considerably higher supply of Au ions to drive branch formation, owing to their larger surfaces. An unfavorable ratio hinders the formation of branches and can result in poorly developed tips (c.f. Figure 2). Therefore, growing NSs from large seeds is a greater challenge and requires growth media with a high precursor concentration, to promote tip growth instead of volume growth. Figure 3f–h shows SEM images of NSs with pointed tips grown with 0.6 mM Au, at positions #2 (red), #5 (green), and #8 (blue).

In summary, we have illustrated a case of combinatorial screening to tune the optical properties to an intended application, for example, excitation at 785 nm. In total, 150 parameter combinations were tested using gradient arrays of substrate-immobilized seeds.

**Molecular Trapping and SERS Biosensing of Pyocyanin.** As a proof-of-concept application, we applied substrates with immobilized NSs for the SERS detection of pyocyanin (Figure 4), a challenging analyte owing to its weak adsorption affinity onto Au surfaces. PCN<sup>-</sup> is a characteristic biomarker for *P. aeruginosa* infections, for example, of the respiratory tract.<sup>40</sup> Apart from being a toxin and promoting virulence in host cells, it participates in intracellular signaling processes.<sup>10</sup> In clinical practice, the concentration of PCN<sup>-</sup> is commonly determined through high-performance liquid chromatography (HPLC), which is time consuming, costly, and laborious.<sup>41</sup> In 1988, Wilson *et al.* reported that clinical sputum samples can contain PCN<sup>-</sup> contents up to  $16.5 \mu\text{g mL}^{-1}$  ( $\approx 8 \times 10^{-5}$  M) for cystic fibrosis patients and up to  $27.3 \mu\text{g mL}^{-1}$  ( $\approx 13 \times 10^{-5}$  M) for patients with bronchiectasis.<sup>42</sup> Similar values of  $8\text{--}50 \times 10^{-5}$  M were found by Hunter *et al.* in cystic fibrosis sputum samples, published in 2012.<sup>43</sup> However, HPLC quantification of phenazines is still challenging owing to difficulties in the assignment and differentiation of chromatographic peaks, as explained and corrected by Glasser *et al.*<sup>44</sup> SERS spectroscopy is a promising and powerful alternative to HPLC analytics. By using substrates with a high density of hotspots formed by collective plasmon modes,<sup>45</sup> micropatterned Au@SiO<sub>2</sub> super-

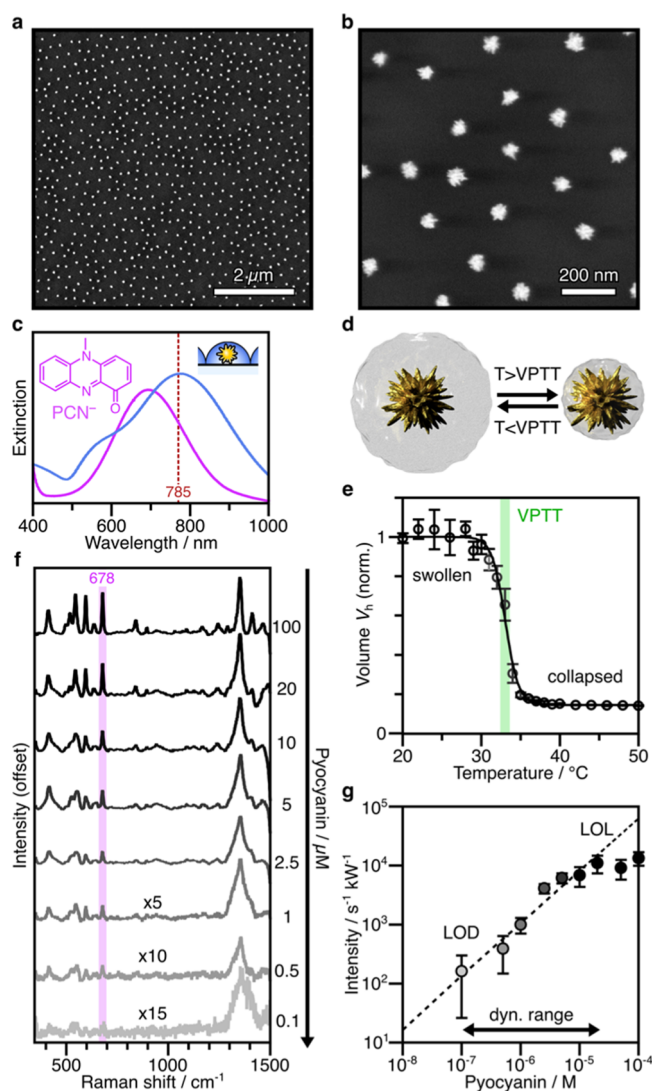


**Figure 4.** Molecular trapping and SERS detection of pyocyanin. SEM images of a substrate-supported array of uniformly distributed isolated NSs in random arrangement at 35,000 $\times$  (a) and 115,000 $\times$  (b) magnifications. (c) Spectral overlap between pyocyanin (violet) and NS array (blue) with the excitation line (785 nm, dashed line). (d) Schematic depiction of thermo-responsive switching between swollen and collapsed pNIPAM shell at the VPTT. (e) Change in hydrodynamic volume measured by DLS. (f) SERS spectra for aqueous pyocyanin solution of decreasing concentrations, in stacked representation. (g) Calibration curve indicating a linear dynamic range between  $10^{-7}$  and  $10^{-5}$  M PCN<sup>-</sup>.

crystal arrays enabled SERS detection of PCN<sup>-</sup> at  $10^{-14}$  M in low-density bacterial cultures at the initial hours of biofilm growth.<sup>10</sup> Later, Žukovskaja and co-workers reported a lab-on-a-chip SERS study and detected concentrations between 1 and  $3 \times 10^{-5}$  M PCN<sup>-</sup> in sputum samples.<sup>40</sup> Their approach built on hotspots formed by induced aggregation of silver colloids, reaching a limit of detection (LOD) as low as  $0.5 \times 10^{-6}$  PCN<sup>-</sup>. Compared to multi-particle arrangements, “sensing pixels” represented by non-coupling single particles offer less “plasmonically active space,” that is, a narrower local distribution of hotspots. For efficient operation, this spatial confinement must be compensated by the efficiency of the individual hotspots.

The blue pigment PCN<sup>-</sup> has a broad absorption band around 700 nm (Figure 4c, violet line), which can be employed for resonant excitation of SERS at 785 nm. For the proof-of-application experiments, we selected the best candidates from the sample pool using maximum SERS efficiency as the main selection criterion (Figure 1h, ≈33 min growth time). Further criteria included a homogeneous distribution of isolated NSs, that is, sufficient spacing between adjacent particles ( $d_{cc} > 2$  effective diameters) and a particle morphology showing branching with pointed tips. The selected samples were immersed overnight at room temperature into aqueous solutions of PCN<sup>-</sup> (0.1–100 μM), followed by washing with water and drying. However, in initial SERS experiments hardly any signal from PCN<sup>-</sup> could be detected, which we attribute to the pNIPAM shells acting as a barrier. To reach the hotspots, PCN<sup>-</sup> must pass through the porous polymer shell and chemisorb onto the core. Owing to the absence of thiol or amine residues, PCN<sup>-</sup> inherently exhibits low affinity for Au surfaces. At the same time, its pronounced hydrophobicity could impede diffusion through the pNIPAM network. At room temperature, pNIPAM is a water-soluble, hydrophilic material with a slight amphiphilic character due to its isopropyl groups. Thus, interactions with domains of lower polarity could compete with gel penetration.<sup>46</sup> However, at temperatures above the volume-phase transition temperature (VPTT, ≈33 °C), the pNIPAM network undergoes an entropic collapse, causing the shell to contract (Figure 4d). DLS measurements between 20 and 50 °C indicated a shrinkage down to 15% of the initial volume above the VPTT (Figure 4e). In conjunction with an increased dispersion of hydrophobic domains, this temperature-induced contraction can be used for molecular trapping of hydrophobic analytes.<sup>24,33</sup>

To promote the chemical accumulation of PCN<sup>-</sup> near the plasmonic cores, we performed a brief tempering above the VPTT. Therefore, 2 μL droplets of analyte solution were deposited onto the surface and heated above 40 °C for 10 min. The robustness of the NSs to this heat treatment was verified by stability tests performed under both wet and dry conditions (Figure S8). After labeling with solutions of concentrations between 10<sup>-7</sup> and 10<sup>-4</sup> M PCN<sup>-</sup>, SERS measurements were performed on a homogeneous array of uniformly distributed isolated NSs (Figure 4a,b; see Figure S9 for large-area SEM images). This single-particle array provided an LSPR band tailored for resonant excitation at 785 nm (Figure 4c, blue line). For each concentration, spectra were averaged from 20 measurements at random locations within the labeled surface area. Figure 4f shows the characteristic fingerprints of the biomarker for decreasing analyte concentrations. The SERS intensity at 678 cm<sup>-1</sup> could be detected within a linear dynamic range of 10<sup>-5</sup> to 10<sup>-7</sup> M (Figure 4g). Within this range, the detected SERS signal changes linearly with analyte concentrations, as required for quantitative analysis. The slope of the calibration curve within the linearity regime corresponds to the sensor's effective sensitivity of ≈10<sup>9</sup> s<sup>-1</sup> kW<sup>-1</sup> M<sup>-1</sup>. The limit of linearity was indicated by the signal remaining almost constant above 2 × 10<sup>-5</sup> M. This upper detection limit is likely due to saturation of the available SERS hotspots at high analyte concentrations. The lower LOD was found to be between 10<sup>-7</sup> and 10<sup>-6</sup> M, which is 1–2 orders of magnitude below PCN<sup>-</sup> concentrations commonly found in clinical samples. The LOD corresponds to the minimum concentration at which the analyte can be reliably detected under the given experimental conditions. However, it can be assumed that by adjusting the

instrumental excitation and light collection efficiency, the LOD could be extended to PCN<sup>-</sup> concentrations below 10<sup>-7</sup> M. These results evidence that the pNIPAM shell, applied as a spacer in the assembly, can co-function as a molecular trap for hydrophobic analytes such as pyocyanin.

Thus, isolated, hydrogel-encapsulated NSs were shown to function as “sensing pixels” for the SERS sensing of a bacterial biomarker at clinically relevant concentrations. Although the detection limit of these single-particle arrays cannot reach the level of sensitivity of multi-particle arrays with higher hotspot densities, the ability to detect sub-μM concentrations of PCN<sup>-</sup> is still remarkable.

## CONCLUSIONS

We have demonstrated the design of plasmonic gradient arrays of anisotropic gold nanoparticles, as a tool for optical tailoring and combinatorial screening of size effects in SERS efficiency. To this end, we have systematically investigated the seeded growth of isolated, non-coupling gold NSs, using substrate-immobilized arrays of seed particles. Arrays of quasi-spherical seeds between 10 and 60 nm were prepared by a lithography-free colloidal approach. By dip-coating seed arrays into different growth solutions, AA/CTAB for isotropic and PVP/DMF for anisotropic overgrowth, particle libraries of NSs were obtained on macroscopic areas (>15 cm<sup>2</sup>, ca. 5 × 10<sup>11</sup> particles/library). Overgrowth was controlled by the local exposure time to the growth solution. This “interrupted growth” by dip-coating allowed us to fabricate gradients over several centimeters (>6 cm), which represent extended particle libraries and reflect the continuous morphological transition from spheres to stars. Such libraries accelerate the investigation of structure–property relations by parallelized production and analysis.

Rapid screening was exemplified by plasmonic tuning of NSs toward resonant excitation at 633 and 785 nm, at which SERS efficiency was found to peak. In addition, the quantitative correlation of SERS activity and optical properties of intermediate states gave detailed insights into the evolution of sensing performance. Such kinetic data evidenced that maximum enhancement is already reached at the end of the initial (fast) growth stage, which corresponds to the development of tips. Subsequent growth does not further improve sensing performance but merely increases the overall size. This connection was presumed before but never proven experimentally. Furthermore, combinatorial screening was demonstrated by investigating the combined influence of seed size and Au precursor content in the growth solution. By parallel processing of a set of 15 gradient arrays, a total of 150 combinations of synthesis parameters could be sampled, each of which would otherwise require separate synthesis and processing. In this way, the stoichiometrically required amount of Au precursor for the targeted growth of tips could be determined for each of the 10 sampled seed sizes. Similar combinatorial experiments could serve as basis for a more sustainable synthesis and optimization of resources.

Lastly, we switched from a model analyte, NTP, to the clinically relevant biomarker PCN<sup>-</sup>. pNIPAM encapsulation was initially found to hinder analyte adsorption, attributed to an incompatibility of the hydrophobic PCN<sup>-</sup> molecules to the hydrophilic shell around the “sensing pixels.” This incompatibility was overcome by exploiting the thermo-responsive nature of pNIPAM and its increased hydrophobicity above the VPTT at 33 °C. By a brief tempering above the VPTT,

encapsulation was rendered into a molecular trap for hydrophobic analytes, promoting the collection of PCN<sup>-</sup> from solution. This allowed for quantitative PCN<sup>-</sup> detection within a linear dynamic range between 10<sup>-5</sup> and 10<sup>-7</sup> M. Thus, isolated, hydrogel-encapsulated NSs may function as “sensing pixels” for the SERS sensing of biomarkers at clinically relevant concentrations.

Our results evidence that particle libraries obtained from gradient seed arrays serve as a tool for kinetic studies, combinatorial parameter screening, parallelized sample processing, and tuning of plasmonic properties. Therefore, we anticipate the methodology presented to be rapidly adopted in the development of alternate designs of advanced sensor devices and nanoparticle-based SERS analysis.

## MATERIALS AND METHODS

**Materials.** HAuCl<sub>4</sub>·3H<sub>2</sub>O (≥99.9%), sodium citrate tribasic dihydrate (≥99%), ascorbic acid (AA; ≥99.9), *N*-isopropylacrylamide (NIPAM; 97%), *N,N'*-methylenebis(acrylamide) (BIS; ≥99.5%; Fluka), potassium peroxodisulfate (≥99.0%; Fluka), sodium dodecyl sulfate (SDS; ≥99.0%), and 3-butenylamine hydrochloride (BA; 97.0%), cetyltrimethylammonium bromide (CTAB; ≥99.9%), H<sub>2</sub>O<sub>2</sub> (35%), isopropanol (≥99.8%), nitrothiophenol (NTP, 99%), poly(ethyleneimine) (PEI, *M*<sub>w</sub> 25 kg mol<sup>-1</sup>, highly branched), poly(*N*-vinylpyrrolidone) (PVP; *M*<sub>w</sub> 10 kg mol<sup>-1</sup>), and pyocyanine (PCN<sup>-</sup>) from *P. aeruginosa* (≥98%) were purchased from Sigma-Aldrich-Merck unless otherwise mentioned. Ethanol absolute (≥98%), NH<sub>4</sub>OH (29% NH<sub>3</sub>), and DMF (synthesis grade) were purchased from VWR Chemicals. All chemicals were used as received. All solutions, except HAuCl<sub>4</sub>·3H<sub>2</sub>O and CTAB, were prepared immediately before use. Purified Milli-Q water was used in all experiments (Millipore, 18.2 MΩ cm). Glassware was washed with *aqua regia* and rinsed extensively with Milli-Q water before use.

**Synthesis of Seed Core/Shell Nanoparticles.** pNIPAM-encapsulated gold nanospheres as seeds were synthesized in two steps, as previously reported.<sup>29</sup> First, quasi-spherical citrate-capped gold nanoparticles of 15 nm in diameter were prepared by citrate reduction.<sup>34</sup> Briefly, 25 mL of a 1 wt % aqueous trisodium citrate dihydrate solution was added quickly during strong magnetic stirring to an aqueous solution of HAuCl<sub>4</sub> (500 mL, 0.5 mM) under heavy boiling. After 15 min, the deep-red colored dispersion was allowed to cool to room temperature. Then, an aqueous SDS solution (3 mL, 0.624 mM) was added dropwise followed by addition of an ethanolic BA solution (0.98 mL, [BA] = 2.88 mM) with a delay of 20 min. The particles were concentrated by centrifugation at 1400 rcf overnight, yielding a stock solution of 0.011 mM Au<sup>0</sup>. Second, the as-prepared nanospheres were encapsulated in pNIPAM shells using free-radical precipitation polymerization. 791 mg of the monomer NIPAM and 161 mg of the cross-linker BIS were dissolved in 200 mL of water in a 250 mL three-neck round-bottom flask. The clear solution was heated to 70 °C and purged with nitrogen. After 15 min of equilibration time, 5 mL of the as-prepared functionalized gold nanoparticle stock solution ([Au<sup>0</sup>] = 0.011 mM) was added dropwise. The polymerization was initiated by the rapid addition of 4 mg of potassium peroxodisulfate dissolved in 1 mL of water. The reaction was allowed to proceed for 2 h under continuous stirring with a magnetic stirrer. The core/shell particles were cleaned by repeated centrifugation/redispersion steps. The final residues were collected, redispersed in approximately 15 mL of water, and freeze-dried.

**Preparation of Substrate-Supported Monolayers of Seed Particles.** Microscopy glass slides (Deltalab; 76 × 26 mm<sup>2</sup>, ref. D100002; or 60 × 24 mm<sup>2</sup>, ref. D102460) were cleaned by 20 min of ultrasound in a mixture of isopropanol and water (3:1, v/v), followed by immersion in a RCA-1 solution (NH<sub>4</sub>OH/H<sub>2</sub>O<sub>2</sub>/H<sub>2</sub>O = 1:1:5, v/v/v) at 70 °C for another 20 min.<sup>47,48</sup> Before and after each cleaning step, the slides were rinsed with water. The freshly cleaned slides were incubated for at least 3 h in an aqueous PEI solution (10 mg mL<sup>-1</sup>) to improve the adhesion of the monolayer on the substrates,<sup>49</sup> washed

with water, dried with N<sub>2</sub> flow, and finally placed on the chuck of a spin coater (Model WS-400B-6NPP; Laurrell Technologies Co). Then, 150 μL of a 1 wt % aqueous dispersion of core/shell particles was evenly distributed on the surface, followed by a ramp of 40 s from 0 to 1000 rpm and further spinning for 90 s. After 5–10 min of curing on an Al foil-covered heating plate set to 100 °C, the substrates were allowed to cool, gently rinsed with water, and dried by N<sub>2</sub> flow.

**Growth of Substrate-Supported Nanospheres.** For the overgrowth of the substrate-supported seed particles, the substrates were dipped into a growth solution and retracted at 1 mm min<sup>-1</sup> using a dip-coater (NadeTech ND-R) at 25 °C maintained by a water bath. The growth solution was prepared by slowly adding 417 μL of HAuCl<sub>4</sub> (0.1 M) to 100 mL of CTAB (0.1 M), followed by dropwise addition of 588 μL of a fresh AA solution (0.1 M), both under vigorous stirring. The substrates were then washed by immersing them twice in water for 1 h and finally dried by N<sub>2</sub> flow. To improve the adhesion of the gradient seed array, substrates were cured for 15 min on an Al foil-covered heating plate set to 100 °C and allowed to cool down.

**Growth of Substrate-Supported NSs.** For the growth of the NSs from substrate-supported seed particles, the substrates were incubated in a PVP/DMF solution (0.1 g mL<sup>-1</sup>) overnight to allow diffusion of PVP to the Au surface. Subsequently, the seed substrates were directly transferred into a fresh growth solution containing 0.275 mM of Au<sup>3+</sup>.<sup>26</sup> The growth solution was prepared by rapid addition of 220 μL of a HAuCl<sub>4</sub> solution (0.126 M) to a PVP/DMF solution (0.1 g mL<sup>-1</sup>; 100 mL) under vigorous stirring. Before immersion, Au<sup>3+</sup> was completely converted to Au<sup>+</sup> within 2 min, as followed by UV/vis spectroscopy using a quartz cuvette and the PVP/DMF solution as background. The growth was performed either by (I) simple immersion into the growth solution (volume 30 mL per substrate) for 30 min or (II) using a dip-coater (immersion 80 mm min<sup>-1</sup>; retraction 1 mm min<sup>-1</sup>, volume 100 mL). Either way, the substrates were finally washed by immersing them twice in EtOH for 1 h and finally dried by N<sub>2</sub> flow. For the simple immersion method, NS growth was performed in a parallelized fashion in 15 centrifuge tubes (27 mm inner diameter) filled with PVP/DMF (10 mM) solution. The volume in each tube was calculated to sum up to 30 mL total volume, in which case the substrate is completely immersed, together with a corresponding amount of precursor solution of gold ions. Pre-reduction of gold ions was performed in a common batch, as described above but adjusted to Au concentration of 0.825 mM. Then, defined amounts of precursor solution were added to the sample tubes to obtain growth solutions with Au concentrations of 0.055, 0.110, 0.165, 0.220, 0.275, 0.330, 0.385, 0.440, 0.495, 0.550, 0.605, 0.660, 0.715, 0.770, and 0.825 mM (final concentration). After 1 min of mixing by vortexing, the substrates were immersed.

**Analyte Labeling.** The substrate-supported arrays were labeled by immersion overnight in freshly prepared aqueous solutions of 1 μM NTP. This analyte solution was prepared using an ethanoic stock solution of NTP (100 mM, which was diluted in two steps to 1 mM and finally to 1 μM). After immersion for 12 h (total volume of 45 mL), the substrate was washed with water and dried by N<sub>2</sub> flow.

**Electron Microscopy.** TEM images were obtained using a LaB<sub>6</sub>-TEM of type JEOL JEM-1400PLUS with an accelerating voltage of 40–120 kV equipped with a GATAN US1000 CCD camera (2k × 2k). Samples were prepared by placing a 2 μL droplet of diluted (nearly colorless) NP dispersions on TEM grids (Cu, 200 Mesh, coated with carbon films; Science Services GmbH). SEM images were obtained using an environmental SEM (FEI Quanta 250 with a Schottky field-emitter gun 0.5–30 kV) with a beam resolution of approx. 1–2.5 nm (secondary electron and backscattered electron detectors, high vacuum) and a dual-beam FEI Helios Nanolab 450FS with a theoretical beam resolution of up to 0.5 nm at 15 kV (circular backscatter detector). To minimize artifacts due to surface charging on the glass substrates, the accelerating voltage was limited to 5 kV for large-area images and to 8–10 kV for detailed images.

**Scanning Probe Microscopy.** Imaging of substrate-supported monolayers was performed with an atomic force microscope (NanoWizard II; JPK Instruments) in the intermittent contact

mode using non-conductive silicon nitride (DNP-S10; Bruker) or antimony-doped silicon cantilevers (TESP-V2, TESPA-V2; Bruker). Data visualization and analysis were carried out using Gwyddion 2.54.<sup>50</sup> The normalized radial distribution function was calculated using the ImageJ plugin "Radial Profile" (v2011-08-22, <http://rsb.info.nih.gov/ij/plugins/radial-profile.html>) by Michael Schmid and Ajay Gopal that applies an autocorrelation of particle centers *via* the Fourier transform.

**Dynamic Light Scattering.** The hydrodynamic radius and  $\xi$ -potential measurements were determined by DLS (Zetasizer Nano ZS system, Malvern Instruments, UK) at scattering angles of 13 and 173° at 25 °C, that is, in the swollen state of the pNIPAM shell. For temperature-dependent experiments between 20 and 50 °C, the sample was equilibrated for 10 min and measured three times at 173°.

**Optical Characterization.** UV/vis/NIR spectra were acquired with a scanning dual-beam spectrophotometer (Cary 5000; Agilent Technologies, Inc.) for solid samples and a single-beam photodiode-array spectrophotometer (Agilent 8453 UV-visible; Agilent Technologies, Inc.) for liquid samples. Solid samples were mounted on a custom-made holder (Ultimaker 3; Ultimaker B.V.) that allowed measurements along the gradient with a spot size of  $2 \times 5 \text{ mm}^2$  in millimeter steps. The extinction at the wavelength of 400 nm (interband transitions),<sup>51</sup> which is assumed to have a size-independent absorption coefficient,<sup>52–55</sup> was used to normalize the UV/vis/NIR spectra and to calculate the molar concentration of Au<sup>0</sup> in the NP dispersions. The molar concentration of Au<sup>0</sup> and the size of the nanoparticles obtained from TEM images enabled the calculation of the particle concentration (number of AuNPs per volume). Time-based kinetical UV/vis/NIR data over the wavelength range of 190–1100 nm were collected at 2 Hz using a scanning double-beam multi-cell spectrophotometer (Cary 3500; Agilent Technologies, Inc.) equipped with a Xe-flash lamp as a light source. Two quartz cuvettes containing solutions of PVP in DMF (4 mL;  $0.1 \text{ mg mL}^{-1}$ ) were continuously stirred by magnetic stirring bars for rapid horizontal and vertical mixing (Spinfin; Aldrich). Next, seed particles were added to the sample cuvette with the other cuvette serving as a reference for background correction. After equilibration at 25 °C, data collection was started followed by the addition of HAuCl<sub>4</sub> (final concentration: 0.275 mM) to the sample cuvette.

**SERS.** Spectra were obtained using a Renishaw inVia reflex equipped with a stigmatic single-pass spectrometer, gratings of 1200 or 1800 grooves  $\text{mm}^{-1}$ , a Peltier-cooled CCD detector, a diode laser (785 nm, 28 mW), and a HeNe laser (633 nm, 7.3 mW) as excitation lines. Spectra were collected using 50× long working-distance objective lens (Zeiss, NA 0.75) by focusing the laser spot at the air/substrate interface, indicated by maximum signal intensity. Each sample was measured by mapping the surface through  $20 \times 20 \mu\text{m}^2$  areas ( $11 \times 11$  points) in equidistant intervals along the gradient direction. For spectral assignment, SERS data were evaluated with reference to spectra of bulk materials acquired by conventional volume Raman.<sup>34</sup> Data analysis and background correction were carried out by multi-peak fitting using Igor Pro 7 (WaveMetrics, Inc., USA).

## ■ ASSOCIATED CONTENT

### SI Supporting Information

The Supporting Information is available free of charge at <https://pubs.acs.org/doi/10.1021/acs.chemmater.1c03223>.

Additional data on the optical, structural, and SERS characterization data (PDF)

## ■ AUTHOR INFORMATION

### Corresponding Authors

**Christian Kuttner** – CIC BiomaGUNE, Basque Research and Technology Alliance (BRTA), Donostia-San Sebastián 20014, Spain; [orcid.org/0000-0002-4093-7469](https://orcid.org/0000-0002-4093-7469); Email: [christian.kuttner@googlemail.com](mailto:christian.kuttner@googlemail.com)

**Luis M. Liz-Marzán** – CIC BiomaGUNE, Basque Research and Technology Alliance (BRTA), Donostia-San Sebastián 20014, Spain; Ikerbasque, Basque Foundation for Science, Bilbao 48009, Spain; Centro de Investigación Biomédica en Red, Bioingeniería, Biomateriales y Nanomedicina (CIBER-BBN), Donostia-San Sebastián 20014, Spain; [orcid.org/0000-0002-6647-1353](https://orcid.org/0000-0002-6647-1353); Email: [lizmarzan@cicbiomagune.es](mailto:lizmarzan@cicbiomagune.es)

### Author

**Valentina Piotto** – CIC BiomaGUNE, Basque Research and Technology Alliance (BRTA), Donostia-San Sebastián 20014, Spain; Nanostructures and Optics Laboratory, Department of Chemical Sciences, University of Padova, Padova 35131, Italy

Complete contact information is available at: <https://pubs.acs.org/doi/10.1021/acs.chemmater.1c03223>

### Author Contributions

The manuscript was written through contributions of all authors. All authors have given approval to the final version of the manuscript.

### Notes

The authors declare no competing financial interest.

## ■ ACKNOWLEDGMENTS

The research leading to these results has received funding from the European Union's Horizon 2020 research and innovation programme under the Marie Skłodowska-Curie grant agreement no. 799393 (NANOBIOME) and was performed under the María de Maeztu Units of Excellence Program from the Spanish State Research Agency (MDM-2017-0720). The authors thank Dr. Judith Langer and Prof. Moreno Meneghetti for scientific discussions, Dr. Evgeny Modin for help with SEM, and Ana Sánchez-Iglesias for help with TEM and for advice on synthesis.

## ■ REFERENCES

- (1) Ziegler, J.; Wörister, C.; Vidal, C.; Hrelescu, C.; Klar, T. A. Plasmonic Nanostars as Efficient Broadband Scatterers for Random Lasing. *ACS Photonics* **2016**, *3*, 919–923.
- (2) Pettine, J.; Choo, P.; Medeghini, F.; Odom, T. W.; Nesbitt, D. J. Plasmonic Nanostar Photocathodes for Optically-Controlled Directional Currents. *Nat. Commun.* **2020**, *11*, 1367.
- (3) Siviš, M.; Pazos-Perez, N.; Yu, R.; Alvarez-Puebla, R.; García de Abajo, F. J.; Ropers, C. Continuous-Wave Multiphoton Photoemission from Plasmonic Nanostars. *Commun. Phys.* **2018**, *1*, 13.
- (4) Langer, J.; Jiménez de Aberasturi, D.; Aizpuru, J.; Alvarez-Puebla, R. A.; Auguie, B.; Baumberg, J. J.; Bazan, G. C.; Bell, S. E. J.; Boisen, A.; Brolo, A. G.; et al. Present and Future of Surface-Enhanced Raman Scattering. *ACS Nano* **2020**, *14*, 28–117.
- (5) Guerrero-Martínez, A.; Barbosa, S.; Pastoriza-Santos, I.; Liz-Marzán, L. M. Nanostars Shine Bright for You. *Curr. Opin. Colloid Interface Sci.* **2011**, *16*, 118–127.
- (6) Reguera, J.; Langer, J.; Jiménez de Aberasturi, D.; Liz-Marzán, L. M. Anisotropic Metal Nanoparticles for Surface Enhanced Raman Scattering. *Chem. Soc. Rev.* **2017**, *46*, 3866–3885.
- (7) Hao, F.; Nehl, C. L.; Hafner, J. H.; Nordlander, P. Plasmon Resonances of a Gold Nanostar. *Nano Lett.* **2007**, *7*, 729–732.
- (8) Liu, Y.; Ashton, J. R.; Moding, E. J.; Yuan, H.; Register, J. K.; Fales, A. M.; Choi, J.; Whitley, M. J.; Zhao, X.; Qi, Y.; et al. A Plasmonic Gold Nanostar Theranostic Probe for In Vivo Tumor Imaging and Photothermal Therapy. *Theranostics* **2015**, *5*, 946–960.
- (9) Espinosa, A.; Reguera, J.; Curcio, A.; Muñoz-Noval, A.; Kuttner, C.; Van de Walle, A.; Liz-Marzán, L. M.; Wilhelm, C. Janus Magnetic-

Plasmonic Nanoparticles for Magnetically Guided and Thermally Activated Cancer Therapy. *Small* **2020**, *16*, 1904960.

(10) Bodelón, G.; Montes-García, V.; López-Puente, V.; Hill, E. H.; Hamon, C.; Sanz-Ortiz, M. N.; Rodal-Cedeira, S.; Costas, C.; Celiksoy, S.; Pérez-Juste, I.; et al. Detection and Imaging of Quorum Sensing in *Pseudomonas aeruginosa* Biofilm Communities by Surface-Enhanced Resonance Raman Scattering. *Nat. Mater.* **2016**, *15*, 1203–1211.

(11) Solís, D. M.; Taboada, J. M.; Obelleiro, F.; Liz-Marzán, L. M.; García de Abajo, F. J. Toward Ultimate Nanoplasmonics Modeling. *ACS Nano* **2014**, *8*, 7559–7570.

(12) Serrano-Montes, A. B.; Langer, J.; Henriksen-Lacey, M.; Jiménez de Aberasturi, D.; Solís, D. M.; Taboada, J. M.; Obelleiro, F.; Sentosun, K.; Bals, S.; Bekdemir, A.; et al. Gold Nanostar-Coated Polystyrene Beads as Multifunctional Nanoprobes for SERS Bioimaging. *J. Phys. Chem. C* **2016**, *120*, 20860–20868.

(13) Solís, D. M.; Taboada, J. M.; Obelleiro, F.; Liz-Marzán, L. M.; García de Abajo, F. J. Optimization of Nanoparticle-Based SERS Substrates through Large-Scale Realistic Simulations. *ACS Photonics* **2017**, *4*, 329–337.

(14) Tran, V.; Thiel, C.; Svejda, J. T.; Jalali, M.; Walkenfort, B.; Erni, D.; Schlücker, S. Probing the SERS Brightness of Individual Au Nanoparticles, Hollow Au/Ag Nanoshells, Au Nanostars, and Au Core/Au Satellite Particles: Single-Particle Experiments and Computer Simulations. *Nanoscale* **2018**, *10*, 21721–21731.

(15) Hrelescu, C.; Sau, T. K.; Rogach, A. L.; Jäckel, F.; Feldmann, J. Single Gold Nanostars Enhance Raman Scattering. *Appl. Phys. Lett.* **2009**, *94*, 153113–153114.

(16) Rodríguez-Lorenzo, L.; Álvarez-Puebla, R. A.; Pastoriza-Santos, I.; Mazzucco, S.; Stéphan, O.; Kociak, M.; Liz-Marzán, L. M.; García de Abajo, F. J. Zeptomol Detection Through Controlled Ultra-sensitive Surface-Enhanced Raman Scattering. *J. Am. Chem. Soc.* **2009**, *131*, 4616–4618.

(17) Meng, X.; Dyer, J.; Huo, Y.; Jiang, C. Greater SERS Activity of Ligand-Stabilized Gold Nanostars with Sharp Branches. *Langmuir* **2020**, *36*, 3558–3564.

(18) Perassi, E. M.; Hrelescu, C.; Wisnet, A.; Döblinger, M.; Scheu, C.; Jäckel, F.; Coronado, E. A.; Feldmann, J. Quantitative Understanding of the Optical Properties of a Single, Complex-Shaped Gold Nanoparticle from Experiment and Theory. *ACS Nano* **2014**, *8*, 4395–4402.

(19) Sanz-Ortiz, M. N.; Sentosun, K.; Bals, S.; Liz-Marzán, L. M. Templated Growth of Surface Enhanced Raman Scattering-Active Branched Gold Nanoparticles within Radial Mesoporous Silica Shells. *ACS Nano* **2015**, *9*, 10489–10497.

(20) Contreras-Cáceres, R.; Sánchez-Iglesias, A.; Karg, M.; Pastoriza-Santos, I.; Pérez-Juste, J.; Pacifico, J.; Hellweg, T.; Fernández-Barbero, A.; Liz-Marzán, L. M. Encapsulation and Growth of Gold Nanoparticles in Thermoresponsive Microgels. *Adv. Mater.* **2008**, *20*, 1666–1670.

(21) Fernández-López, C.; Pérez-Balado, C.; Pérez-Juste, J.; Pastoriza-Santos, I.; de Lera, Á. R.; Liz-Marzán, L. M. A General LbL Strategy for the Growth of PNIPAM Microgels on Au Nanoparticles with Arbitrary Shapes. *Soft Matter* **2012**, *8*, 4165–4170.

(22) Litti, L.; Reguera, J.; García de Abajo, F. J.; Meneghetti, M.; Liz-Marzán, L. M. Manipulating Chemistry through Nanoparticle Morphology. *Nanoscale Horiz.* **2020**, *5*, 102–108.

(23) Rauh, A.; Honold, T.; Karg, M. Seeded Precipitation Polymerization for the Synthesis of Gold-Hydrogel Core-Shell Particles: The Role of Surface Functionalization and Seed Concentration. *Colloid Polym. Sci.* **2015**, *294*, 37–47.

(24) Mueller, M.; Tebbe, M.; Andreeva, D. V.; Karg, M.; Alvarez-Puebla, R. A.; Pazos-Perez, N.; Fery, A. Large-Area Organization of PNIPAM-Coated Nanostars as SERS Platforms for Polycyclic Aromatic Hydrocarbons Sensing in Gas Phase. *Langmuir* **2012**, *28*, 9168–9173.

(25) Demille, T. B.; Hughes, R. A.; Dominique, N.; Olson, J. E.; Rouvimon, S.; Camden, J. P.; Neretina, S. Large-Area Periodic Arrays

of Gold Nanostars Derived from HEPES-, DMF-, and Ascorbic-Acid-Driven Syntheses. *Nanoscale* **2020**, *12*, 16489–16500.

(26) Barbosa, S.; Agrawal, A.; Rodríguez-Lorenzo, L.; Pastoriza-Santos, I.; Alvarez-Puebla, R. A.; Kornowski, A.; Weller, H.; Liz-Marzán, L. M. Tuning Size and Sensing Properties in Colloidal Gold Nanostars. *Langmuir* **2010**, *26*, 14943–14950.

(27) Sánchez-Iglesias, A.; Aldeanueva-Potel, P.; Ni, W.; Pérez-Juste, J.; Pastoriza-Santos, I.; Alvarez-Puebla, R. A.; Mbenkum, B. N.; Liz-Marzán, L. M. Chemical Seeded Growth of Ag Nanoparticle Arrays and Their Application as Reproducible SERS Substrates. *Nano Today* **2010**, *5*, 21–27.

(28) Giner-Casares, J. J.; Henriksen-Lacey, M.; García, I.; Liz-Marzán, L. M. Plasmonic Surfaces for Cell Growth and Retrieval Triggered by Near-Infrared Light. *Angew. Chem., Int. Ed.* **2016**, *55*, 974–978.

(29) Müller, M. B.; Kuttner, C.; König, T. A. F.; Tsukruk, V. V.; Förster, S.; Karg, M.; Fery, A. Plasmonic Library Based on Substrate-Supported Gradiational Plasmonic Arrays. *ACS Nano* **2014**, *8*, 9410–9421.

(30) Sindram, J.; Volk, K.; Mulvaney, P.; Karg, M. Silver Nanoparticle Gradient Arrays: Fluorescence Enhancement of Organic Dyes. *Langmuir* **2019**, *35*, 8776–8783.

(31) König, M.; Radojčić, A.; Schlücker, S.; Xie, W. Label-free SERS Monitoring of Hydride Reduction Catalyzed by Au Nanostars. *J. Raman Spectrosc.* **2016**, *47*, 1024–1028.

(32) Brasse, Y.; Müller, M. B.; Karg, M.; Kuttner, C.; König, T. A. F.; Fery, A. Magnetic and Electric Resonances in Particle-to-Film-Coupled Functional Nanostructures. *ACS Appl. Mater. Interfaces* **2018**, *10*, 3133–3141.

(33) Álvarez-Puebla, R. A.; Contreras-Cáceres, R.; Pastoriza-Santos, I.; Pérez-Juste, J.; Liz-Marzán, L. M. Au@pNIPAM Colloids as Molecular Traps for Surface-Enhanced, Spectroscopic, Ultra-Sensitive Analysis. *Angew. Chem., Int. Ed.* **2008**, *48*, 138–143.

(34) Kuttner, C.; Höller, R. P. M.; Quintanilla, M.; Schnepf, M. J.; Dulle, M.; Fery, A.; Liz-Marzán, L. M. SERS and Plasmonic Heating Efficiency from Anisotropic Core/Satellite Superstructures. *Nanoscale* **2019**, *11*, 17655–17663.

(35) Höller, R. P. M.; Kuttner, C.; Mayer, M.; Wang, R.; Dulle, M.; Contreras-Cáceres, R.; Fery, A.; Liz-Marzán, L. M. Colloidal Superstructures with Triangular Cores: Size Effects on SERS Efficiency. *ACS Photonics* **2020**, *7*, 1839–1848.

(36) Höller, R. P. M.; Jahn, I. J.; Cialla-May, D.; Chanana, M.; Popp, J.; Fery, A.; Kuttner, C. Biomacromolecular-Assembled Nanoclusters: Key Aspects for Robust Colloidal SERS Sensing. *ACS Appl. Mater. Interfaces* **2020**, *12*, 57302–57313.

(37) Pazos-Perez, N.; Guerrini, L.; Alvarez-Puebla, R. A. Plasmon Tunability of Gold Nanostars at the Tip Apexes. *ACS Omega* **2018**, *3*, 17173–17179.

(38) Zhang, Y.; Walkenfort, B.; Yoon, J. H.; Schlücker, S.; Xie, W. Gold and Silver Nanoparticle Monomers Are Non-SERS-Active: A Negative Experimental Study with Silica-Encapsulated Raman-Reporter-Coated Metal Colloids. *Phys. Chem. Chem. Phys.* **2015**, *17*, 21120–21126.

(39) Song, H.-M.; Wei, Q.; Ong, Q. K.; Wei, A. Plasmon-Resonant Nanoparticles and Nanostars with Magnetic Cores: Synthesis and Magnetomotive Imaging. *ACS Nano* **2010**, *4*, 5163–5173.

(40) Žukovskaja, O.; Jahn, I. J.; Weber, K.; Cialla-May, D.; Popp, J. Detection of *Pseudomonas aeruginosa* Metabolite Pyocyanin in Water and Saliva by Employing the SERS Technique. *Sensors* **2017**, *17*, 1704.

(41) Fernández, R. O.; Pizarro, R. A. High-Performance Liquid Chromatographic Analysis of *Pseudomonas aeruginosa* Phenazines. *J. Chromatogr. A* **1997**, *771*, 99–104.

(42) Wilson, R.; Sykes, D. A.; Watson, D.; Rutman, A.; Taylor, G. W.; Cole, P. J. Measurement of *Pseudomonas aeruginosa* Phenazine Pigments in Sputum and Assessment of Their Contribution to Sputum Sol Toxicity for Respiratory Epithelium. *Infect. Immun.* **1988**, *56*, 2515–2517.

(43) Hunter, R. C.; Klepac-Ceraj, V.; Lorenzi, M. M.; Grotzinger, H.; Martin, T. R.; Newman, D. K. Phenazine Content in the Cystic Fibrosis Respiratory Tract Negatively Correlates with Lung Function and Microbial Complexity. *Am. J. Respir. Cell Mol. Biol.* **2012**, *47*, 738–745.

(44) Glasser, N. R.; Hunter, R. C.; Liou, T. G.; Newman, D. K. Refinement of Metabolite Detection in Cystic Fibrosis Sputum reveals HEME correlates with Lung Function Decline. *PLoS One* **2019**, *14*, No. e0226578.

(45) Hamon, C.; Novikov, S.; Scarabelli, L.; Basabe-Desmonts, L.; Liz-Marzán, L. M. Hierarchical Self-Assembly of Gold Nanoparticles into Patterned Plasmonic Nanostructures. *ACS Nano* **2014**, *8*, 10694–10703.

(46) Pelton, R. Poly(N-Isopropylacrylamide) (PNIPAM) is never Hydrophobic. *J. Colloid Interface Sci.* **2010**, *348*, 673–674.

(47) Kuttner, C.; Tebbe, M.; Schlaad, H.; Burgert, I.; Fery, A. Photochemical Synthesis of Polymeric Fiber Coatings and Their Embedding in Matrix Material: Morphology and Nanomechanical Properties at the Fiber-Matrix Interface. *ACS Appl. Mater. Interfaces* **2012**, *4*, 3484–3492.

(48) Kuttner, C.; Hanisch, A.; Schmalz, H.; Eder, M.; Schlaad, H.; Burgert, I.; Fery, A. Influence of the Polymeric Interphase Design on the Interfacial Properties of (Fiber-Reinforced) Composites. *ACS Appl. Mater. Interfaces* **2013**, *5*, 2469–2478.

(49) Steiner, A. M.; Mayer, M.; Seuss, M.; Nikolov, S.; Harris, K. D.; Alexeev, A.; Kuttner, C.; König, T. A. F.; Fery, A. Macroscopic Strain-Induced Transition from Quasi-Infinite Gold Nanoparticle Chains to Defined Plasmonic Oligomers. *ACS Nano* **2017**, *11*, 8871–8880.

(50) Nečas, D.; Klapetek, P. Gwyddion: An Open-Source Software for SPM Data Analysis. *Cent. Eur. J. Phys.* **2012**, *10*, 181–188.

(51) Bastús, N. G.; Comenge, J.; Puntès, V. Kinetically Controlled Seeded Growth Synthesis of Citrate-Stabilized Gold Nanoparticles of up to 200 nm: Size Focusing versus Ostwald Ripening. *Langmuir* **2011**, *27*, 11098–11105.

(52) Rodríguez-Fernández, J.; Pérez-Juste, J.; Mulvaney, P.; Liz-Marzán, L. M. Spatially-Directed Oxidation of Gold Nanoparticles by Au(III)-CTAB Complexes. *J. Phys. Chem. B* **2005**, *109*, 14257–14261.

(53) Hendel, T.; Wuithschick, M.; Kettemann, F.; Birnbaum, A.; Rademann, K.; Polte, J. In Situ Determination of Colloidal Gold Concentrations with UV–Vis Spectroscopy: Limitations and Perspectives. *Anal. Chem.* **2014**, *86*, 11115–11124.

(54) Hendel, T.; Wuithschick, M.; Kettemann, F.; Birnbaum, A.; Rademann, K.; Polte, J. Correction to In Situ Determination of Colloidal Gold Concentrations with UV–Vis Spectroscopy: Limitations and Perspectives. *Anal. Chem.* **2015**, *87*, 5846–5847.

(55) Scarabelli, L.; Sánchez-Iglesias, A.; Pérez-Juste, J.; Liz-Marzán, L. M. A “Tips and Tricks” Practical Guide to the Synthesis of Gold Nanorods. *J. Phys. Chem. Lett.* **2015**, *6*, 4270–4279.